

Are stripped envelope supernovae really deficient in ⁵⁶Ni?

RYOMA OUCHI,¹ KEIICHI MAEDA,¹ JOSEPH P. ANDERSON,² AND RYO SAWADA³

¹*Department of Astronomy, Kyoto University, Kitashirakawa-Oiwake-cho, Sakyo-ku, Kyoto 606-8502, Japan*

²*European Southern Observatory, Alonso de Córdova 3107, Casilla 19, Santiago, Chile*

³*Department of Astrophysics and Atmospheric Sciences, Faculty of Science, Kyoto Sangyo University, Motoyama, Kamigamo, Kita-ku, Kyoto 603-8555, Japan*

Submitted to ApJ

ABSTRACT

The nuclear decay of ⁵⁶Ni is one of the most important power sources of supernovae (SNe). Recent works have indicated that the ⁵⁶Ni masses estimated for Stripped Envelope SNe (SESNe) are systematically higher than those estimated for SNe II. Although this may suggest a distinct progenitor structure or explosion mechanism between these types of SNe, the possibility remains that this may be caused by observational bias. One important possible bias is that SESNe with low ⁵⁶Ni mass are dim, and therefore they are more likely to escape detection. By investigating the distributions of the ⁵⁶Ni mass and distance for the samples collected from the literature, we find that the current literature SESN sample indeed suffers from a significant observational bias, i.e., objects with low ⁵⁶Ni mass - if they exist - will be missed, especially at larger distances. This suggests that the different ⁵⁶Ni masses between SNe II and SESNe may be, at least partially, explained by this observational bias. We also conducted mock observations assuming that the ⁵⁶Ni mass distribution for SESNe is intrinsically the same with that for SNe II. We find that the ⁵⁶Ni distribution of the detected SESNe samples moves toward higher mass than the assumed intrinsic distribution, because of the difficulty in detecting low-⁵⁶Ni mass (low-luminosity) SESNe. These results could explain the general trend of the higher ⁵⁶Ni mass distribution (than SNe II) of SESNe found thus far in the literature. However, further clear examples of low-⁵⁶Ni mass SESNe ($\leq 0.01M_{\odot}$) are required to add weight to this hypothesis.

Keywords: stars: massive — supernovae: general

1. INTRODUCTION

Core collapse supernovae (SNe) are the explosions of massive stars, marking the termination of their lives. A small fraction of the gravitational energy of the collapsing iron core is converted into the kinetic and thermal energy of the ejected matter (Woosley et al. 2002). Core collapse SNe are classified into several categories, based on their spectra and light curves. SNe with hydrogen lines in their spectra are classified as Type II SNe (SNe II), while those lacking hydrogen lines are called Type I SNe (SNe I). Among SNe I, those having He lines are called Type Ib SNe (SNe Ib) and those lacking He lines are called SNe Ic. Type IIb supernovae (SNe IIb) are

characterized by hydrogen lines in their early phase spectra which gradually disappear, and by the He lines which become increasingly strong at later phases (Filippenko 1997). SNe IIb, Ib and Ic are considered to originate from massive stars that have lost a significant fraction of the envelope during their evolution, and thus they are collectively called Stripped Envelope SNe (SESNe) (Smartt et al. 2009).

It has been established that SNe IIP are the explosions of red supergiants based on light curve models (Falk & Arnett 1977; Elmhamdi et al. 2003; Bersten et al. 2011) and also from the direct detection of the progenitors on pre-SN images (Smartt 2009, 2015). On the contrary, the progenitors of SESNe are more uncertain. For SNe IIb/Ib/Ic, two possible progenitor channels have been proposed. One is a massive WR star (with the main-sequence mass $M_{\text{ms}} \gtrsim 25M_{\odot}$) that has blown off the H-rich envelope by its own stellar wind (Georgy 2012;

Gräfener & Vink 2016). The other is a relatively low mass star which loses its envelope by mass transfer to a binary companion (Podsiadlowski et al. 1992; Stancliffe & Eldridge 2009). Recent observational evidence favors the latter scenario. The light curve modeling and direct progenitor detection indicate that the progenitors are relatively low mass stars ($M_{\text{ms}} \lesssim 18M_{\odot}$), being consistent with the binary scenario (Maund et al. 2011; Bersten et al. 2014; Van Dyk et al. 2014; Folatelli et al. 2015). Also, for some SESNe, companion star candidates are detected, which indicates a binary origin (Maund et al. 2004; Folatelli et al. 2014).

One of the most important power sources of SNe is newly synthesized ^{56}Ni . ^{56}Ni decays into ^{56}Co , and then into ^{56}Fe . This nuclear decay chain powers the tail phase of SNe II and the entire light curve of SESNe. The ^{56}Ni masses of SNe have been estimated using several methods (Anderson 2019). For SNe II, the tail luminosity has mostly been used to estimate the ^{56}Ni mass, assuming the complete trapping of γ -rays produced from the nuclear decay. For SESNe, on the contrary, the tail luminosity cannot be easily used due to the incomplete trapping of the γ -ray photons, and the ‘Arnett-rule’ has often been used instead (Arnett 1982; Wheeler et al. 2015). This rule dictates that the peak luminosity of SESNe should be equal to the instantaneous energy deposition rate by the nuclear decay. For both types of SNe, the mass of synthesized ^{56}Ni has also been estimated from light curve modeling (Utrobin & Chugai 2011; Bersten et al. 2014).

Interestingly, mounting evidence has been accumulating to show that the masses of synthesized ^{56}Ni of the observed SESNe are systematically higher than those of SNe II. This result was first formally outlined by Kushnir (2015). After that, Anderson (2019) collated the ^{56}Ni masses for 258 SNe from the published literature and compared the ^{56}Ni mass distributions for various types of SNe. He found that the ^{56}Ni masses estimated for SNe II are systematically lower than SESNe. The median of the ^{56}Ni masses is $0.032M_{\odot}$ for SNe II, $0.102M_{\odot}$ for SNe IIB, $0.163M_{\odot}$ for SNe Ib, $0.155M_{\odot}$ for SNe Ic, and $0.369M_{\odot}$ for SNe Ic-broad line (SNe Ic-BL). Thus, SESNe have higher ^{56}Ni masses than SNe II.

This result has important implications. The production of ^{56}Ni is sensitive to the explosion mechanism (Maeda & Tominaga 2009; Suwa & Tominaga 2015; Sawada & Maeda 2019) and the progenitor mass (Suwa et al. 2019). If we assume a binary origin for SESNe progenitors, the core structure should be similar between SESNe and SNe II. Thus, we would expect that the ^{56}Ni mass distributions are also similar. That is, assuming a binary origin for SESNe progenitors, the progenitors of

SESNe and SNe II are expected to share similar range in the initial progenitor mass. Moreover, the binarity mainly affects the outer envelope but not the core structure (Yoon et al. 2010, 2017; Ouchi & Maeda 2017). Solving the problem of different ^{56}Ni masses between SESNe and SNe II should help to clarify the progenitors of SESNe.

Before concluding that the systematically different ^{56}Ni mass between SESNe and SNe II may be caused by a different structure in the progenitor cores, systematic errors in calculating the ^{56}Ni masses should be addressed (Anderson 2019). Subsequently, several works have concluded that even by taking into account the different methods to derive the ^{56}Ni mass and various observational errors, a difference in ^{56}Ni masses between SNe II and SESNe remains (Meza & Anderson 2020; Afsariardchi et al. 2020). Meza & Anderson (2020) however noted the possibility that SESNe with a small amount of ^{56}Ni might have been missed by the existing surveys. Since the luminosity of SESNe is mostly powered by the radioactive decay of ^{56}Ni , the SESNe with the lowest ^{56}Ni masses are the faintest (Lyman et al. 2016). Thus, they can possibly escape from detection depending on the survey depth. On the contrary, SNe II with a small amount of ^{56}Ni can still power themselves by diffusion of the thermal energy coming from the explosion energy. Thus, SNe II can more easily be detected than SESNe, even if the ^{56}Ni mass is small. Indeed, several Ni-poor SESNe ($M_{\text{Ni}} \lesssim 0.02M_{\odot}$) have been detected (Kasliwal et al. 2010; Shivvers et al. 2016; Nakaoka et al. 2019). However, it should also be noted that none of these examples are low-luminosity canonical SESNe as they all show unusual properties.

The aim of this paper is to investigate how much observational bias may lie in the ^{56}Ni mass distribution of the samples collected from the published literature. In section 2, we define the samples that are used throughout the paper. Section 3 describes some equations that are used in this paper. In section 4, we investigate whether there is an observational bias in the ^{56}Ni mass distribution of our data samples by examining the relation between distance, luminosity and ^{56}Ni mass. In section 5 and section 6, we conduct mock observations of SESNe and theoretically investigate the effect of observational bias on the ^{56}Ni mass distribution. We discuss the results in section 7 and finally conclude the paper in section 8.

2. DATA SAMPLE

In this section, we describe the observational samples used in this paper. Throughout the paper, we use the samples of ^{56}Ni estimates collected from the published

literature both for SESNe and SNe II. Anderson (2019) recently compiled such samples, including 143 SESNe and 115 SNe II. Specifically, he used the SAO/NASA ADS astronomy query form¹, searching for articles with “supernova” and “type II” that were published until August 2018, then “supernova” and “type IIB” and so forth in manuscript abstracts. Then, he identified those publications with published ⁵⁶Ni mass estimates. In addition to this sample, we add newly published objects between August 2018 and November 2020. The newly added reference list can be found at the end of this manuscript. Note that we do not include ⁵⁶Ni estimates that are derived from combined models, such as ‘magnetar + ⁵⁶Ni model’ or ‘circumstellar interaction + ⁵⁶Ni model’ (e.g. Gangopadhyay et al. 2020). We name these final samples ‘LS-SESNe (Large Sample SESNe)’ and ‘LS-SNeII (Large Sample SNe II)’, respectively. The sample sizes are 187 and 115² for LS-SESNe and LS-SNeII, respectively.

In the case of SESNe, we also use a different sample, which we call ‘Meza-SESNe’; this is the same sample as that used in Meza & Anderson (2020). Those authors defined a SESN sample with well-sampled photometry at optical and near-IR wavelengths. This led to a sample of 37 events. The references for these samples are shown in Meza & Anderson (2020).

In section 4.2, in order to compare the luminosity function between SESNe and SNe II, we use the sample of 57 SNeII taken from Hamuy (2003); Müller et al. (2017); Pejcha & Prieto (2015). These events have published values of the mid-plateau phase luminosity. These papers are included in the reference list of Anderson (2019), and thus, this is a sub-sample of LS-SNeII. We call this small sample ‘SS-SNeII (Small Sample SNe II)’.

For all these objects, we adopt the distance to the host galaxy from the redshift independent measurement in NED³. In case there is no redshift independent measurement of the distance to the host, we adopt the Hubble distance on NED, which includes the correction of Virgo, GA, and Shapley. If the host was anonymous or the distance was not found in NED, we take the distance from the individual published literature.

3. THE RELATIONS USED IN THIS PAPER

¹ <https://ui.adsabs.harvard.edu/classic-form>

² The size of LS-SNeII is the same as the sample of Anderson (2019). This occurred because this time we excluded objects with only upper or lower limits for the ⁵⁶Ni mass. The number of thus removed events was by chance equal to that of the newly added events.

³ <https://ned.ipac.caltech.edu>

3.1. The relations for the peak luminosity and the timescale of SESNe

Two important quantities that characterize the light curves of SESNe are the the peak luminosity (L_p) and the time it takes from the explosion to the peak (t_p). In the following analyses of this paper, we require the relations that connect these values to the ⁵⁶Ni mass.

For a given ⁵⁶Ni mass, the peak luminosity is estimated from the formula shown in Stritzinger & Leibundgut (2005), which is based on the ‘Arnett-rule’. This rule assumes that the peak luminosity (L_p) of a SN powered by the decay of ⁵⁶Ni is equal to the instantaneous energy deposition rate by radioactive decay at that time:

$$L_p = 10^{43} \times (M_{\text{Ni}}/M_{\odot}) \times (6.45 \times e^{-t_p/8.8} + 1.45 \times e^{-t_p/111.3}) [\text{ergs}^{-1}]. \quad (1)$$

Next, we assume that t_p equals to the diffusion timescale, τ_m . Although this assumption is not exactly correct, it is a good approximation (Lyman et al. 2016).

$$t_p \approx \tau_m \equiv \left(\frac{\kappa}{\beta c} \right)^{1/2} \left(\frac{6M_{\text{ej}}^3}{5E_K} \right)^{1/4} = 8.407 \times \left(\frac{M_{\text{ej}}}{M_{\odot}} \right)^{3/4} \left(\frac{E_K}{10^{51} \text{erg}} \right)^{-1/4} [\text{day}] \quad (2)$$

β is a constant of integration and the value is ≈ 13.7 , and we assume $\kappa = 0.07 \text{ g cm}^{-2}$ for the opacity.

The ejecta mass and kinetic energy, M_{ej} and E_K , of SESNe are known to be highly correlated with the ⁵⁶Ni mass (Lyman et al. 2016). Using Fig. 8 in Lyman et al. (2016) in the linear scale, we fit the data by linear regression. Note that we removed the data of SNe Ic-BL from their figures, since they are quite unusual objects. Thus, we derive,

$$M_{\text{ej}}/M_{\odot} = 7.10 \times M_{\text{Ni}}/M_{\odot} + 1.40, \quad (3)$$

$$E_K/10^{51} \text{erg} = 3.90 \times M_{\text{Ni}}/M_{\odot} + 0.83. \quad (4)$$

Combining equation 1 with equations 2, 3 and 4, we can estimate the peak luminosity for a given ⁵⁶Ni mass.

3.2. Observable distance for a given luminosity

Now that we know the peak luminosity of a SESN for a given ⁵⁶Ni mass, it is also important to know out to what distance we can detect it assuming a fixed limiting magnitude. For this purpose, we use the relation in Hamuy (2003):

$$\log D_{\text{lim}} [\text{cm}] = \frac{1}{5} \times (2.5 \log L [\text{ergs}^{-1}] + V_{\text{lim}} - A_t + BC + 8.14). \quad (5)$$

Here, V_{lim} is the limiting magnitude in the V band, D_{lim} is the limiting distance, A_t is the total extinction and BC is the bolometric correction. For simplicity, we assume zero both for A_t and BC . Using this relation, we can calculate the observable distance for a given luminosity, assuming a fixed limiting magnitude.

4. INVESTIGATING OBSERVATIONAL BIAS IN THE DATA SAMPLE

In this section, we investigate whether there is an observational bias in the ^{56}Ni mass distribution of our data samples by examining the relation between distance, luminosity and ^{56}Ni mass.

4.1. ^{56}Ni mass and distance

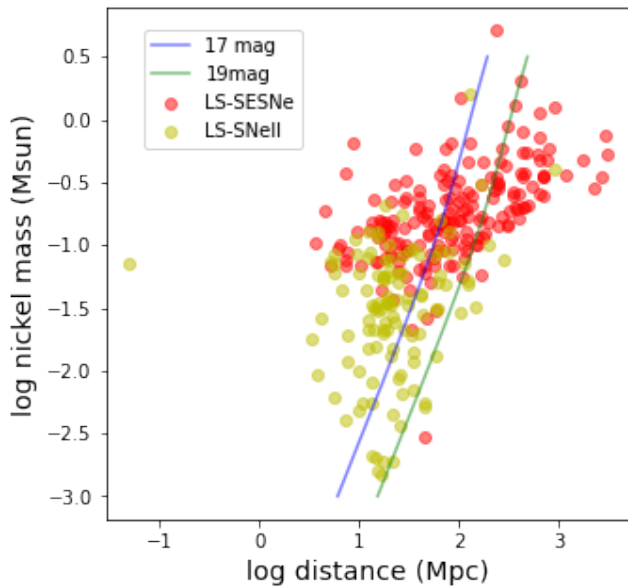


Figure 1. The ^{56}Ni masses of our samples as a function of the distance. The red points refer to LS-SESNe, while yellow points refer to LS-SNeII. For reference, the limiting distance for a given ^{56}Ni mass estimated in section 3 is also shown for the case of limiting magnitude of $V_{\text{lim}} = 17$ (blue) and 19 mag (green).

In order to clarify how the observational biases may affect the ^{56}Ni mass distribution in our samples, we look at the ^{56}Ni mass of our samples as a function of the distance. Figure 1 shows the ^{56}Ni masses of our samples plotted as a function of the distance. It can be seen that there is a strong trend that the ^{56}Ni mass decreases as the distance decreases for SESNe. This suggests that the objects with low ^{56}Ni masses (i.e. dim objects) and large distance, if they exist, may be missed. It is, however, important to emphasize that we are still lacking the SESNe with low ^{56}Ni mass ($\log M_{\text{Ni}}(M_{\odot}) \lesssim -1.7$:

i.e., $M_{\text{Ni}} \lesssim 0.02M_{\odot}$) even at small distance (\log distance (Mpc) $\lesssim 1$). For SNe II, even though the ^{56}Ni mass slightly decreases as the distance decreases, the effect is much less significant than SESNe.

These trends can be confirmed by looking at Fig 2 and 3. Figure 2 shows how the ^{56}Ni mass distribution changes when we take different sizes of volume-limited samples. It is expected that the ^{56}Ni mass distribution approaches to the intrinsic distribution as we take the volume-limited sample at a closer location. It is seen that the ^{56}Ni mass distribution of SESNe significantly shifts to the lower mass when we take the smaller volume-limited sample⁴. On the contrary, SNe II do not change notably for the different sizes of volume-limited sample. From this, we can infer that the LS-SESNe may not trace the intrinsic ^{56}Ni mass distribution, while LS-SNeII nearly do.

Figure 3 shows the average ^{56}Ni mass in the volume-limited samples plotted as a function of the threshold distance. This figure, again, shows that LS-SESNe suffer from a significant observational bias and the discrepancy between SESNe and SNe II becomes smaller as we take the smaller volume-limited sample, and finally becomes within a factor of three.

Figure 4 compares the distance distribution between LS-SESNe and LS-SNeII. We can see that the distance distribution is closer for SNe II than SESNe. Meza & Anderson (2020) showed that their 35 SESNe sample, excluding two Ic-GRB objects, have the mean distance (46.7 Mpc) similar to that of their SNe II sample (42.7 Mpc). However, our significantly larger sample of LS-SESNe has the mean distance of 226.6 Mpc, while LS-SNeII has the mean distance of 41.5 Mpc. Even if we remove Ic-BL and Ic-GRB from the SESNe sample, the mean distance is 99.8 Mpc, which is more than twice the value of LS-SNeII. This indicates that the SESNe samples are collected at more distant locations than SNe II, where the objects suffer from more significant observational bias, supporting the results derived above.⁵

4.2. Luminosity distribution

In this section, we investigate the luminosity distribution of our samples. We emphasise that the analysis

⁴ Note, however, that the distributions for the lowest 20% of the ^{56}Ni masses are nearly the same for these different sizes of volume-limited samples. This may indicate that the lack of canonical SESNe with relatively low ^{56}Ni mass ($\lesssim 0.02M_{\odot}$) is real. We will further discuss it in section 7.

⁵ Although the samples in Meza & Anderson (2020) were taken at small distances ($\approx 40 - 50$ Mpc), the SESNe with low ^{56}Ni mass ($\lesssim 0.02M_{\odot}$) were still lacking. Thus, the lack of canonical SESNe with relatively low ^{56}Ni mass ($\lesssim 0.1M_{\odot}$) may actually be real. We will further discuss this point in section 7.

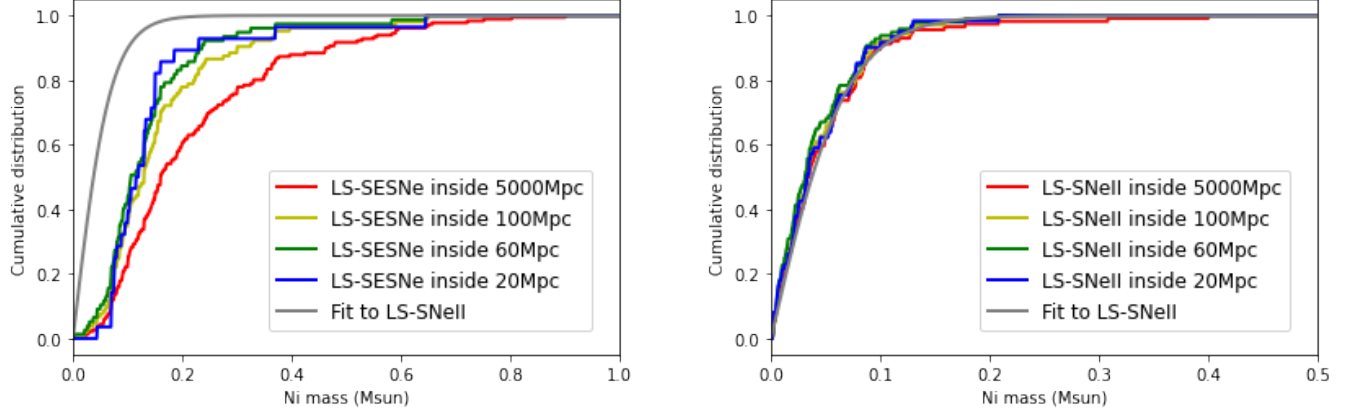


Figure 2. Left: The ^{56}Ni mass distribution of LS-SSESNe for the different sizes of volume-limited samples. The red cumulative distribution shows the ^{56}Ni mass distribution of the samples among LS-SSESNe whose distances are less than 5000 Mpc, while yellow, green and blue cumulative distributions show those whose distances are less than 100 Mpc, 60 Mpc and 20 Mpc, respectively. Right: The same figure as on the left plotted for LS-SNeII. For both figures, the non-linear least square fit to the LS-SNe II cumulative distribution is also shown with a gray line (See sec 5.1 for more detail).

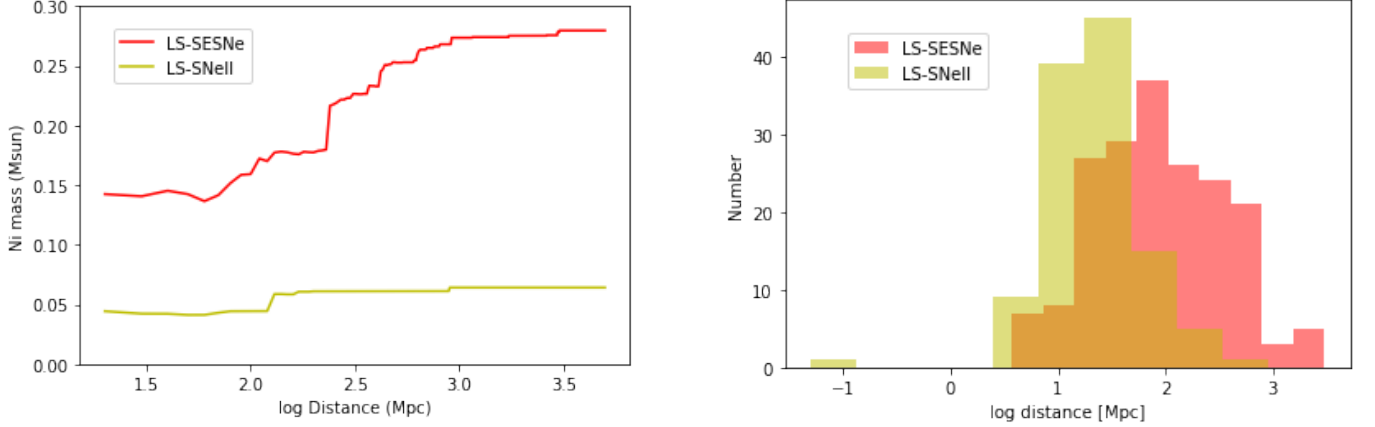
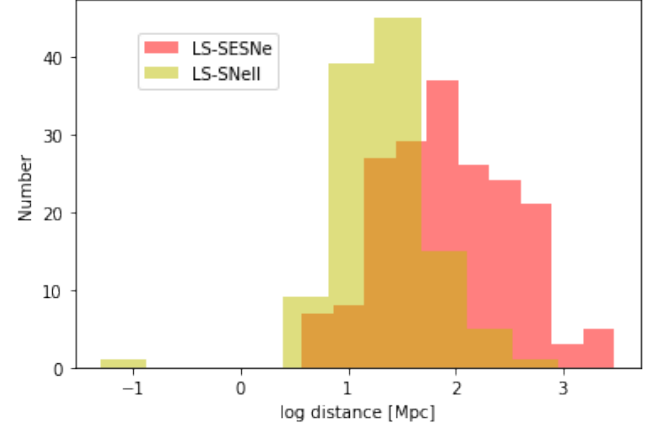


Figure 3. The average ^{56}Ni mass in the volume-limited sample plotted as a function of the threshold distance from 20 Mpc to 5000 Mpc. The red line refers to LS-SSESNe sample, while yellow line refers to LS-SNeII.

Figure 4. The comparison of the distance distributions of LS-SSESNe (red) and LS-SNeII (yellow).



in this section is not affected by the assumption about the relation between the ^{56}Ni masses and the peak luminosity of SESNe. As noted in section 2, here, we only use the sample of 57 SNeII taken from Hamuy (2003); Müller et al. (2017); Pejcha & Prieto (2015), which we call SS-SNeII. Note that Hamuy (2003) only publishes the V-band magnitude, so, we convert it to bolometric luminosity assuming the bolometric correction to be zero, following Goldberg et al. (2019). For SESNe, we use the sample of 37 from Meza-SESNe.

The left panel of Fig. 5 shows the luminosity distribution as a function of distance for these samples. For SESNe we show the peak luminosity, while we show the plateau luminosity for SNe II. There is a positive correlation between the luminosity and distance both for

SESNe and SNe II. Also, the minimum luminosity for a fixed distance is similar between SNe II and SESNe. This indicates that both of our samples may be suffering from the same observational selection effect. The right panel of Fig. 5 compares the luminosity functions of SESNe and SNe II. We notice that there is a luminosity cut off for both types at around $\log L[\text{erg s}^{-1}] \sim 41.7$. The SNe II plateau phase and the SESNe peak phase are powered by the different physical mechanisms, with the former powered by the explosion energy and the latter powered by the radioactive decay of ^{56}Ni . It is true the plateau luminosity and the ^{56}Ni mass of SNe II are known to be positively correlated (Pejcha & Prieto 2015), but it is unlikely that the lower luminosity cut off are the same between the two groups of SNe just in terms of physics. Thus, we speculate that this simultaneous cut off of the luminosity functions for both

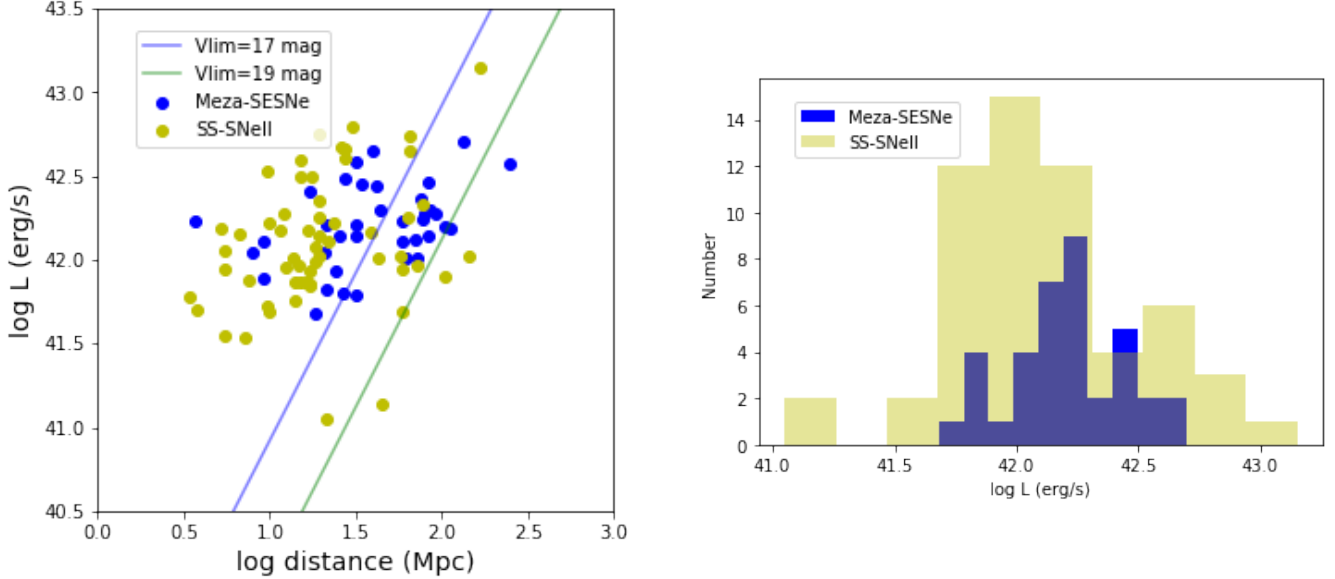


Figure 5. Left: The distributions of the peak luminosity of SESNe (blue points) and plateau luminosity of SNe II (yellow points) plotted as a function of distance. For reference, the limiting luminosity as a function of distance is plotted for the case of limiting magnitude of $V_{\text{lim}} = 17$ (blue line) and 19 mag (green line), respectively. Right: The comparison of the luminosity function of SESNe (blue) and SNe II (yellow) sample. For SESNe, we show the peak luminosity, and for SNeII, we show the plateau luminosity.

types of SNe is caused by an observational selection effect. This selection effect will introduce a bias in the ^{56}Ni mass distribution for SESNe, as the ^{56}Ni mass is closely connected to their peak luminosities.

To summarize, the results derived in section 4 all point to the following interpretation: *The ^{56}Ni mass of SESNe samples collected from the published literature suffer from notable observational bias, i.e. the distant objects with relatively low ^{56}Ni mass are missed, meaning that the samples are biased towards the luminous objects. On the contrary, the ^{56}Ni masses of SNe II samples suffer much less from such bias.* We, again, emphasise that the analyses in this section are not affected by the assumption about the relation between the ^{56}Ni masses and the peak luminosity of SESNe⁶.

5. METHOD OF MOCK OBSERVATIONS

In the previous sections, we have found that the ^{56}Ni mass distribution in our SNe II sample is not notably suffering from the observational bias. Therefore, below, we start additional analysis based on the following two working hypotheses: (1) The ^{56}Ni mass distribution in

our SNe II sample (LS-SNeII) represents the intrinsic ^{56}Ni mass distribution of SNe II, and (2) SESNe have the same intrinsic ^{56}Ni mass distribution as that of SNe II. The second assumption is based on the hypothesis that assuming a binary origin for SESNe, progenitors of SESNe and SNe II are expected to share the similar range in the initial mass (see section 1)⁷.

Based on these hypotheses, we conduct mock observations of SESNe. By comparing the results of mock observations to the data sample, we discuss the reliability of these hypotheses. In the rest of this section, we describe the procedure of the mock observation in more detail.

5.1. ^{56}Ni mass distribution

As noted above, here we assume that the intrinsic ^{56}Ni mass distribution of SESNe is the same as the ^{56}Ni mass distribution of LS-SNe II. To simplify the numerical analyses, we fit the cumulative histogram of ^{56}Ni mass (denoted here as $f(x)$) by the function of $f(x) = \tanh(a_0 \times x)$, using non-linear least squares. We obtained $a_0 = 14.60$ as the best fit parameter. The comparison of our fitted curve with our sample is shown in Fig. 6. Below, we use the function of $f(x) =$

⁶ We note, however, that Meza & Anderson (2020) have shown that the statistical difference of ^{56}Ni mass between SESNe and SNe II remains even if they take relatively close samples ($\approx 40-50$ Mpc). Thus, the observational bias alone may not be sufficient to explain all of the statistical difference in the ^{56}Ni mass (section 7).

⁷ Note, however, that there are indications that the progenitors of SESNe may be more massive than SNe II either as an entire class or for the particular SN Ic class (e.g. Anderson et al. 2012; Valenti et al. 2012; Fang et al. 2019).

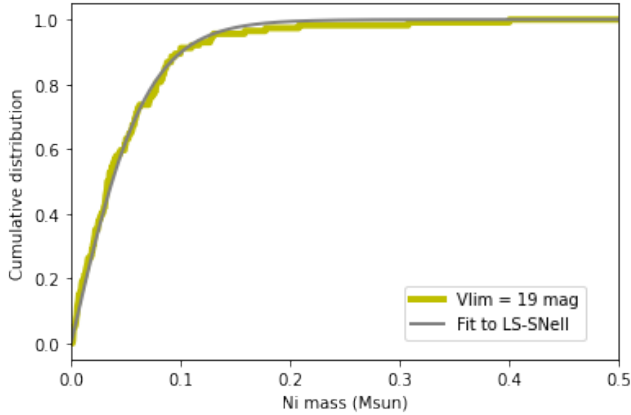


Figure 6. The cumulative ^{56}Ni mass distribution of LS-SNeII and the non-linear least squares fit to it, assuming the function of $f(x) = \tanh(a_0 \times x)$.

381 $\tanh(14.60 \times x)$ to represent the ^{56}Ni mass distribution
382 of SESNe.

5.2. Simulating the observations

384 We simulate one SESN by selecting the ^{56}Ni mass and
385 distance from the given probability distributions. We
386 select a value of ^{56}Ni mass from the distribution derived
387 in section 5.1. Then, for each ^{56}Ni mass thus derived, the
388 distance is randomly chosen following the probability
389 function of $p \propto (\text{distance})^3$, i.e., the volume size. The
390 range of distance is set from zero up to the limiting
391 distance corresponding to the peak luminosity of SESNe
392 with a ^{56}Ni mass of $1.0M_{\odot}$.

393 For each object with a given ^{56}Ni mass and distance,
394 we decide whether to add it to the ‘detected’ sample or
395 not based on the following procedure. First, from the
396 given ^{56}Ni mass, we estimate the peak luminosity as de-
397 scribed in 3. Next, we can estimate the limiting distance
398 using equation 5, for the peak luminosity derived above.
399 If the selected distance is within the observable distance
400 corresponding to its peak luminosity, we consider it to
401 be detected and add it to the detected sample. Other-
402 wise, we consider that the object escapes detection and
403 do not add it to the detected sample. Once the number
404 of detections reaches 100, we stop one iteration of the
405 mock observation. The number of 100 is chosen to be
406 consistent with the order of magnitude of our LS-SESNe
407 sample size. Note, however, that only in section 6.1, we
408 set this number as 37 (i.e., the Meza-SESNe sample size)
409 in order to make a direct comparison to Meza-SESNe.
410 We iterate the procedure described above 10^3 times, in
411 order to clarify the possible range of the distributions
412 by taking into account the statistical fluctuation due to
413 the limited sample size.

6. RESULTS OF MOCK OBSERVATION

6.1. Luminosity function

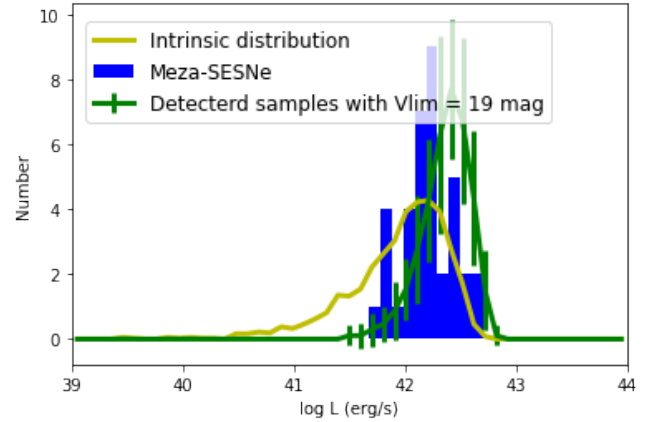


Figure 7. The luminosity functions derived from the mock observation are compared to the luminosity function of Meza-SESNe (blue). The yellow histogram is the distribution of the detected samples in the mock observation assuming that all objects are detected regardless of their distances, i.e; this traces the intrinsic luminosity function of SESNe (assuming that this is the same as that of SNeII). The green histogram is the luminosity function of the detected sample in the mock observation, assuming the limiting magnitude of 19 mag. For the green line, the solid line represents the mean distribution of 1000 iterations of 37 detections and the error bar is the standard deviation of 1000 distributions in each bin.

416 Here, we show the results of the mock observation
417 described in section 5. We assume a fixed limiting mag-
418 nitude of 19 mag in this section. Figure 7 compares the
419 luminosity functions derived from the mock observations
420 to the luminosity function of Meza-SESNe⁸. Here, in or-
421 der to make the direct comparison to Meza-SESNe, we
422 stop one iteration of mock observation when the num-
423 ber of detected objects reaches 37 (i.e., the Meza-SESNe
424 sample size), not 100. Then, we repeat this 1000 times
425 to clarify the possible range of the distributions.

426 Interestingly, we can see that the luminosity function
427 in the ‘detected’ samples is shifted to high luminosity
428 compared to the model intrinsic luminosity function.
429 Since the objects with higher luminosity (i.e., higher
430 ^{56}Ni mass) have the larger observable volume, they do-
431 minates the detected sample. It is also worthwhile to note
432 that the luminosity function of our detected samples in
433 the mock observation roughly explains the observed lu-
434 minosity function of Meza-SESNe. Especially, the lower
435 cut-off at around $\log L \sim 41.7$ is naturally obtained.

⁸ The reason for the non-smooth intrinsic distribution in Fig. 7 is the small number (i.e., 37) of detections we assumed.

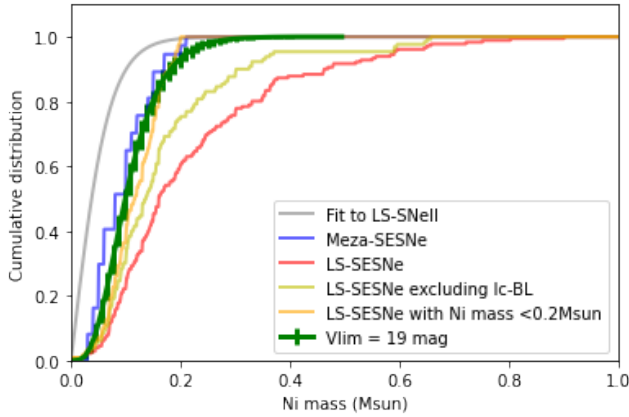
6.2. ^{56}Ni mass distribution

Figure 8. The ^{56}Ni mass distribution in the detected sample of our mock observation (green) is compared to Meza-SESNe (blue) and LS-SESNe (red). The ^{56}Ni mass in Meza-SESNe is the value estimated using the ‘Arnett-rule’. The green solid line represents the mean distribution of 1000 iterations of 100 detections and the error bar is the standard deviation of 1000 iterations in each bin. For reference, a sub-sample derived from LS-SESNe by removing Ic-BL is colored with yellow, while a sub-sample of LS-SESNe which satisfies $M_{\text{Ni}} \leq 0.2M_{\odot}$ is colored with orange. Also, the fit to the ^{56}Ni mass distribution of LS-SNe II is shown with a gray line.

Figure 8 compares the cumulative ^{56}Ni mass distribution in the detected samples to different data samples. Note that, below, we stop one iteration of mock observation when the number of detect objects reaches 100. The ^{56}Ni mass distribution in the detected sample of our mock observation is skewed to higher mass compared to the assumed intrinsic distribution. This is due to the observational bias, being consistent with the shift of the luminosity function discussed in the previous section. The predicted ^{56}Ni mass distribution is very close to that of Meza-SESNe, which consists of well-observed objects. From this, we again emphasize that the systematically high ^{56}Ni masses in the SESNe sample compared to those of SNe II sample could, at least partly, be explained by the observational bias.

The larger sample LS-SESNe, however, contains more massive objects than Meza-SESNe, which are not explained by our mock observations. If we remove the objects with $M_{\text{Ni}} \gtrsim 0.2M_{\odot}$ from LS-SESNe, it matches with the prediction of mock observations much better. This might indicate that the objects with $M_{\text{Ni}} \gtrsim 0.2M_{\odot}$ are triggered by a different explosion mechanism from the objects with lower ^{56}Ni masses (see section 7).

6.3. Effect of different limiting magnitudes

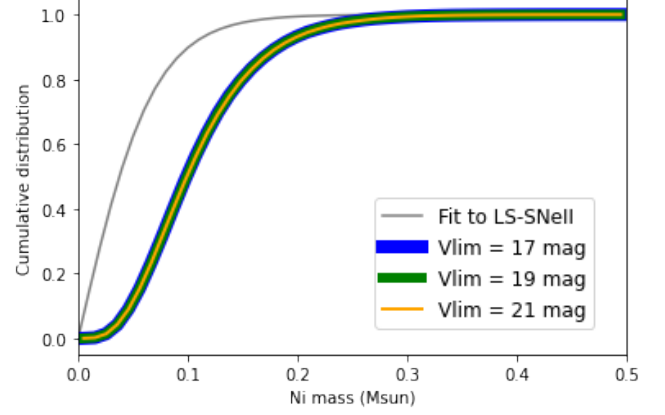


Figure 9. The cumulative ^{56}Ni mass distribution of the detected samples in the mock observation for the different limiting magnitudes. Blue, green, orange lines refer to the limiting magnitude of 17 mag, 19 mag, and 21 mag, respectively. Each line is the mean of the distributions derived from 1000 iterations. For reference, the fit to the ^{56}Ni mass distribution of LS-SNe II is shown with a gray line.

In the previous section, we have assumed a limiting magnitude of $V_{\text{lim}} = 19$ mag. Next, we will see how the different values of the limiting magnitudes affect our results. In Fig. 9, we show the ^{56}Ni mass distribution of the detected samples in the mock observation for the different limiting magnitudes. We can see that the ^{56}Ni mass distribution is quite insensitive to the different values of the limiting magnitudes. This can be explained as follows. The ^{56}Ni mass distribution in the observed sample can be derived by multiplying the assumed intrinsic distribution of ^{56}Ni mass by $D_{\text{lim}}(M_{\text{Ni}})^3$. Here, $D_{\text{lim}}(M_{\text{Ni}})$ is the limiting distance calculated using equation 5. Thus, the term of V_{lim} only changes the scale of the ^{56}Ni mass distribution, but does not affect the normalized distribution. Thus, we can say that the results derived in the previous section is robust to the different limiting magnitudes that are assumed.

In Fig. 10, we show the distance distribution of the detected samples in the mock observation for the different limiting magnitudes. We can see that the distance distribution is sensitive to the different value of the limiting magnitude. The higher the limiting magnitude is, the observable volume becomes larger. Thus, the more distant objects dominates the observed sample.

In the right panel of Fig. 11, the ^{56}Ni masses and distances of the detected samples for the different limiting magnitudes are over-plotted onto Fig. 1. As discussed above, the objects with low ^{56}Ni mass are lacking compared to the assumed intrinsic distribution, which is consistent with the data samples. However, it is important to note that our predictions from the mock observations

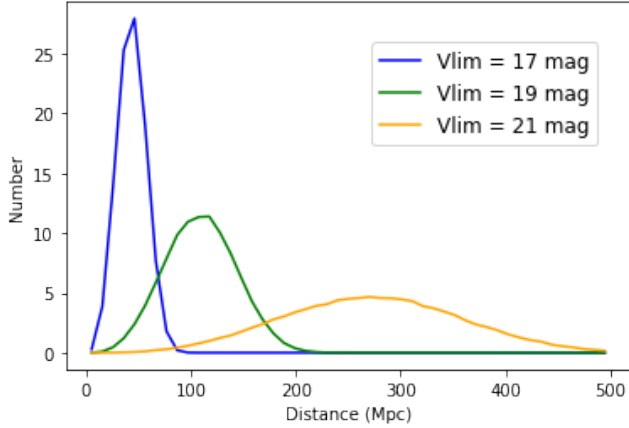


Figure 10. The distance distribution of the detected samples in the mock observation for the different limiting magnitudes. Blue, green, orange lines refer to the limiting magnitude of 17 mag, 19 mag, and 21 mag, respectively. Each line is the mean of the distributions derived from 1000 iterations.

fail to explain the high ^{56}Ni masses of $\gtrsim 0.2M_{\odot}$ that exist in the data samples collected from the published literature as already noted in section 6.2.

6.4. Effects of different observational cadences

So far, we implicitly assumed an infinitely small observational cadence in the mock observation. This means that an object is always detected as long as its peak luminosity exceeds the observational limiting magnitudes. However, existing surveys have a wide range of observational cadence from hours to a few tens of days, depending on their scientific aims. Therefore, some objects may be missed due to infrequent observations, even if the peak luminosity exceeds the observational limiting magnitudes. Therefore, here we attempt to take this into account. Following this, we investigate how the different observational cadences affects our results. We fix the limiting magnitude as 19.0 mag in this section for simplicity.

To proceed with this investigation, we take a simplified approach. We assume that the peak luminosity is maintained for the duration of t_p calculated using equation 2. For the ejecta mass and explosion energy that appear in equation 1 and 2, we use the relations in equation 3 just as we have done in the analyses so far. We simulate the values of observational cadence of 0.0, 10.0, 20.0, 30.0 days. In the mock observation, we add a procedure as follows, in order to decide whether an object is detected or not: if the duration of the event is less than the observational cadence, we add it to the observed sample with the probability of $p = t_p/t_{\text{cadence}}$. If the duration of the event is longer than the observational cadence, we con-

sider the object is detected and add it to the observed sample.

Figure 12 compares the ^{56}Ni mass distribution of the detected samples for the different observational cadences. It is seen that the difference is negligible. This is because the timescale of SESNe within our formalism is not particularly sensitive to the ^{56}Ni mass as shown in Fig. 13. Thus, we conclude that our results are robust to the different assumptions about the observational cadences. However, note that Fig. 13 is based on the linear fitting equations 4. This fitting is done using the samples with ^{56}Ni masses above $0.03M_{\odot}$, and the validity of the linear extrapolation to the lower ^{56}Ni masses is not trivial (see, section 7).

7. DISCUSSION

In section 4, we found that the ^{56}Ni masses of SESNe samples collected from the published literature suffer from notable observational bias, while those of SNe II samples suffer from much less bias. This may be because: (1) SNe II samples are collected at closer distances compared to SESNe samples (Fig. 4), meaning that the former suffer less bias; or (2) the luminosity of SESNe have higher dependence on the ^{56}Ni mass than SNe II. Indeed, the peak luminosity of SESNe is theoretically expected to follow $L_{\text{peak}} \propto M_{\text{Ni}}$ (Arnett 1982), while the mid-plateau luminosity of SNe II is phenomenologically known to follow $L_{\text{plateau}} \propto M_{\text{Ni}}^{0.65}$ (Pojucha & Prieto 2015). Moreover, at the early phase, SNe II generally have higher luminosity than the mid-plateau phase. Thus, the detectability of SNe II is affected much less by ^{56}Ni mass than SESNe.

We have conducted mock observations and shown that if we assume that the intrinsic ^{56}Ni mass distribution of SESNe is the same as that of LS-SNe II, the ^{56}Ni mass distribution of SESNe in the detected samples becomes more massive compared to the assumed intrinsic distribution, which is very close to the distribution of Meza-SESNe. This indicates that even if a significant number of SESNe with low ^{56}Ni masses (i.e. similar to those low ^{56}Ni SNe II masses) exists, we would find difficulty in detecting them and thus they would be significantly underrepresented in current literature samples.

However, some problems still remain to be solved. It is true that our mock observations predict that the detection of SESNe is dominated by relatively luminous objects. But, there should be at least a few SESNe with low ^{56}Ni mass, $M_{\text{Ni}} \lesssim 0.02M_{\odot}$, especially at small distances, considering that many SNe II with such low ^{56}Ni masses are detected. However, in our samples, very few SESNe have been found with such low ^{56}Ni mass. Of course, it may indicate that SESNe with such low ^{56}Ni

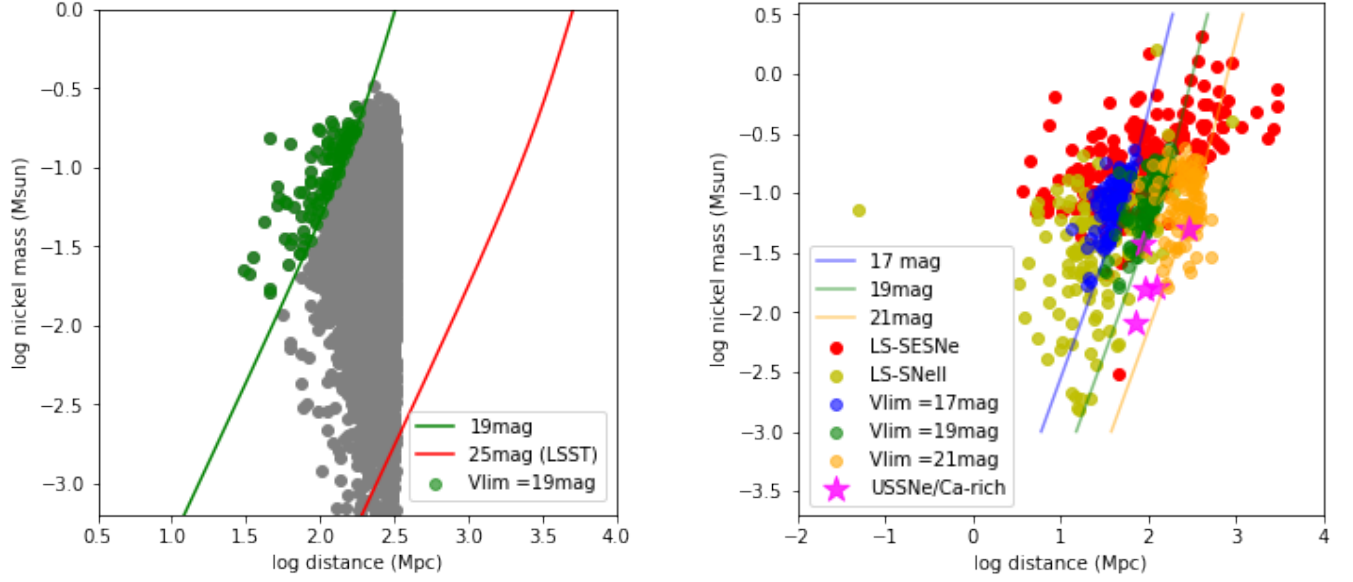


Figure 11. Left: The ^{56}Ni mass and distance of the detected samples in one iteration (i.e., 100 detections) for the limiting magnitudes of 19 mag. Gray points are all the events that were randomly picked up until the number of detections reached 100. For reference, the limiting distance for a given ^{56}Ni mass estimated as in section 3 are also shown assuming the limiting magnitudes of 19 (green) and 25 (red) mag. The latter represents the limiting magnitude for the single-visit depth in LSST (Ivezic et al. 2019). Right: The ^{56}Ni mass and distance of the detected samples in one iteration for the different limiting magnitudes. Blue, green, orange points refer to the case of limiting magnitude of 17 mag, 19 mag, and 21 mag, respectively. We add the ultra-stripped envelope SNe (USSNe) candidates with magenta star marks (see section 7 for a discussion of these events). The references for USSNe are listed at the end of the manuscript. For both panels, the limiting distance for a given ^{56}Ni mass estimated as in section 3 are also shown assuming the fixed limiting magnitudes.

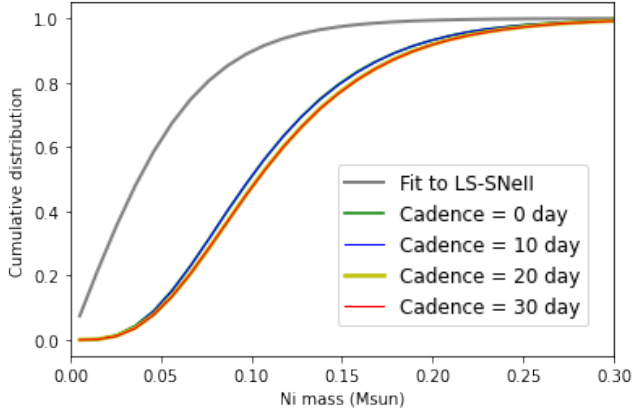


Figure 12. The ^{56}Ni mass distribution of the detected samples for the different observational cadences. Green, blue, yellow, and red points refer to the cadence of 0.0, 10.0, 20.0, 30.0 days, respectively. Each line is the mean of the distributions derived from 1000 iterations. For reference, the fit to the ^{56}Ni mass distribution of LS-SNe II is shown with a gray line.

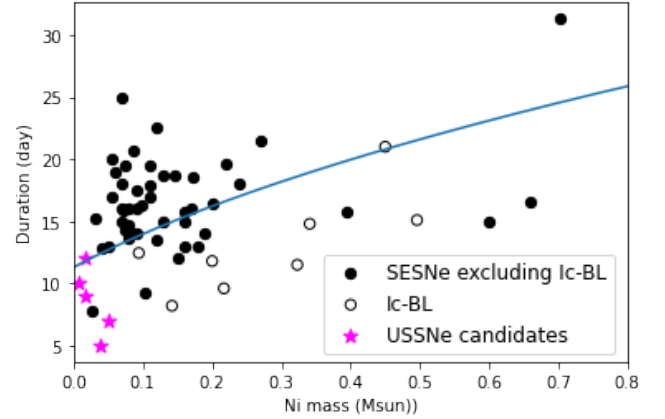


Figure 13. The estimated duration of SESNe using equation 2 plotted as a function of ^{56}Ni mass. For reference, the observational data taken from Lyman et al. (2016) and Prentice et al. (2019) are also shown with black points. Among them, open circles are the SNe Ic-BL, while the filled circles are the other types of SESNe. Also, the data of USSNe candidates are also shown with magenta star marks, which are taken from the reference list attached at the end of the manuscript.

masses actually do not exist and the statistical difference of ^{56}Ni mass between SESNe and SNe II is real. But, it may also be possible that the SESNe with low ^{56}Ni mass

do not appear as canonical SESNe and instead appear as peculiar objects which are difficult to detect.

First, such low- ^{56}Ni mass SESNe may be related to the so called rapidly evolving transients. As shown in Fig. 13, the ^{56}Ni mass and the timescale of SESNe are known to be positively correlated: i.e., SESNe with lower ^{56}Ni mass are expected to have shorter timescales. If we remove the SNe Ic-BL, which are considered to be quite different from the other types of SESNe, the timescale of SESNe decreases more rapidly than our prediction (Fig. 13). Thus, our linear fit (section 3.1) may not be valid at small ^{56}Ni masses, and it can be possible that SESNe with low ^{56}Ni mass ($\lesssim 0.02M_{\odot}$) are observed as rapidly evolving transients with timescales shorter than 10 days⁹ Actually, SN 2017czd in our sample is a SN IIB with very small ^{56}Ni mass of $0.003M_{\odot}$. This object is classified also as a rapidly evolving transient (Nakaoka et al. 2019). Drout et al. (2014) have estimated that the rate of rapidly evolving transients is 4-7 % of the core collapse SNe rate. Since the fraction of SESNe in the core collapse SNe is 36.6 % (Smith et al. 2011), the rapidly evolving transients occupy 11-19 % of SESNe. This number is comparable to the fraction of SESNe with $M_{\text{Ni}} \lesssim 0.01M_{\odot}$ assuming the same ^{56}Ni mass distribution as LS-SNeII. Since the events with short timescales ($\lesssim 10$ days) can be easily missed, this hypothesis may be consistent with the lack of SESNe with low ^{56}Ni masses ($\lesssim 0.02M_{\odot}$)¹⁰

The SESNe with low ^{56}Ni mass may also originate from the so-called ultra-stripped envelope SNe (USSNe). Actually, the ejecta mass and ^{56}Ni mass of SESNe are known to be positively correlated (Lyman et al. 2016). Thus, the ejecta mass of the SESNe with low ^{56}Ni mass are expected to be small. In Fig. 11, the USSNe candidates are also shown. They have the ^{56}Ni mass lower than most of our SESNe sample. Theoretical calculations also indicate that USSNe should synthesize quite low ^{56}Ni of $\sim 0.01M_{\odot}$ (Suwa et al. 2015; Moriya et al. 2017). Specifically, SN2019dge, an USSNe candidate, has an estimated ^{56}Ni mass of $0.017M_{\odot}$ (Yao et al. 2020), which is quite low. The rate of such events is estimated as 2-12% of core collapse supernova: i.e., 5.6-33.3% of SESNe (Smith et al. 2011). This number is con-

sistent with the fraction of SESNe with $M_{\text{Ni}} \lesssim 0.02M_{\odot}$ under the distribution we assumed. Furthermore, the timescale of USSNe candidates are known to be short ($\lesssim 10$ days), which is much less than our prediction (Fig. 13). Such short-timescale objects may be systematically non-detected in the existing surveys as noted in the previous paragraph. Note, however, that the ^{56}Ni masses of USSNe candidates discovered so far are in general not too low: i.e., many SNe II have been detected with ^{56}Ni mass lower than these objects. Therefore, these objects alone may not be sufficient to explain the deficit of SESNe with low ^{56}Ni mass.

The SESNe with low ^{56}Ni mass may also have the possible link to SNe Ibn, which are not included in our samples. SN Ibn is a explosion characterized by He emission line that is considered to originate from the interaction with the He-rich material. These objects are considered to eject less ^{56}Ni than the bulk of other SESNe (Moriya & Maeda 2016).

It is also important to note that our predictions from the mock observations fail to explain the high ^{56}Ni masses of $\gtrsim 0.2M_{\odot}$, which occupy a significant fraction of LS-SESNe (sections 6.2 and 6.3). One possibility for this is that such objects with high ^{56}Ni mass are triggered by a different explosion mechanism from the objects with lower ^{56}Ni masses. Actually, as shown in Fig. 8, the mock observation explains the data sample much better, if we remove the objects with $M_{\text{Ni}} \gtrsim 0.2M_{\odot}$ from LS-SESNe. Note that SNe Ic-BL, whose ^{56}Ni mass is significantly higher than the rest of SESNe (Anderson 2019), are considered to be triggered by a different explosion mechanism from the other types of SESNe (Lazzati et al. 2012; Barnes et al. 2018). Thus, the objects with $M_{\text{Ni}} \gtrsim 0.2M_{\odot}$ might be triggered by the similar mechanism as Ic-BL. The fraction of objects with $M_{\text{Ni}} \gtrsim 0.2M_{\odot}$ among LS-SESNe is 42 %, while that of Ic-BL is 30 %, which are not so different.

The difference in the ^{56}Ni mass can also be caused by a different initial mass range of SESNe progenitors from that of SNe II. Current observational evidence favors the scenario that the mass stripping in SNe IIB/Ib progenitor is caused by binary mass transfer rather than the extensive stellar wind of a massive star ($M_{\text{ms}} \gtrsim 25M_{\odot}$) (Woosley et al. 1994; Benvenuto et al. 2013; Folatelli et al. 2015). However, there are several indications that at least a fraction of SESNe progenitors may be more massive than those of SNe II (e.g. Anderson et al. 2012; Maund 2018; Fang et al. 2019). This may imply that our assumption that SESNe share the same ^{56}Ni mass distribution as SNe II may be too simplified.

Another possibility is that different amounts of fall back may occur between SNe II and SESNe. SNe II

⁹ Note, that some of the rapidly evolving transient are known to be difficult to explain by only considering the radioactive decay model (e.g. Drout et al. 2014). However, the properties of the rapidly evolving the transients are diverse (Pursiainen et al. 2018) and there are many that are compatible with the radioactive decay scenario.

¹⁰ Note, that most of the rapidly evolving transient discovered so far have ^{56}Ni mass of $\gtrsim 0.03M_{\odot}$ (Drout et al. 2014; Pursiainen et al. 2018; Tampo et al. 2020). However, considering that the number of samples detected so far is limited (≈ 100) (Pursiainen et al. 2018), it is natural that they are dominated by the relatively luminous objects as we have shown in section 6.

have the thick hydrogen envelope outside the He core, and the shock is decelerated while crossing the envelope. Thus, it is expected that SNe II suffer from fall back of the inner material more substantially than SESNe. In this case, the ^{56}Ni mass distribution of SNe II we have used may be a lower limit (Sawada et al. in prep).

Throughout the paper, we have contrasted the SNe II to SESNe in general. Anderson (2019) has suggested that there may be difference of the ^{56}Ni mass distribution even among the different types of SESNe. Especially, SNe IIB seem to have smaller ^{56}Ni than SNe Ib/Ic. This might be explained in that SNe IIB can be detected more easily than SNe Ib/Ic due to their cooling emission. However, investigating this possibility quantitatively is beyond the scope of this paper.

When deep surveys like LSST are deployed in the future, we can test our hypotheses. In the left panel of Fig. 11, we show the detection limit for a limiting magnitude of 25 mag, representing the single-visit depth in LSST (Ivezic et al. 2019). We can see that basically all the SESNe with low ^{56}Ni masses ($\lesssim 0.02M_{\odot}$) are detected if they occur closer than ≈ 100 Mpc¹¹. Thus, we will be able to construct a complete sample of SESNe in the local universe. With such a sample, we can test whether the lack of SESNe with $\lesssim 0.02M_{\odot}$ is real or not.

8. CONCLUSION

The nuclear decay of ^{56}Ni is one of the most important power sources of supernovae (SNe). Recent works have indicated that the ^{56}Ni masses estimated for SESNe are systematically higher than those estimated for SNe II. Although this may indicate distinct progenitor structure or explosion mechanism between these types of SNe, the possibility remains that this may be caused by observational biases.

By investigating the distributions of ^{56}Ni mass and distance for the data samples collected from the litera-

ture, we have found that SESNe samples suffer from significant observational bias; objects with low ^{56}Ni masses may be systematically missed, especially at larger distances. Thus, this work has elucidated that the observational bias must be taken into account in discussing the different ^{56}Ni masses between SNe II and SESNe.

We also conducted mock observations assuming that the intrinsic ^{56}Ni mass distribution of SESNe is the same as the ^{56}Ni mass distribution of SNe II collected from the literature. We have found that the ^{56}Ni distribution for the detected samples of SESNe becomes more massive compared to the assumed intrinsic distribution due to the observational bias. This result may, at least partially, explain the lack of low ^{56}Ni mass objects in the SESNe data sample collected from the literature. Although this result relies on the assumption noted above, this supports that at least a part of the systematically different ^{56}Ni masses between these types of SNe are due to the observational bias.

We emphasize, however, that the SESNe with low ^{56}Ni mass ($\lesssim 0.02M_{\odot}$) are still lacking even at small distances ($\lesssim 30$ Mpc). This may indicate that the observational bias alone may not be sufficient to explain all of the statistical difference between SESNe and SNe II. Another possibility is that the SESNe with low ^{56}Ni mass appear as either rapidly evolving transients or ultra-stripped SNe, which are difficult to detect due to their short timescales.

9. ACKNOWLEDGEMENT

R.O. acknowledges support provided by Japan Society for the Promotion of Science (JSPS) through KAKENHI grant (19J14158). K.M. acknowledges support provided by Japan Society for the Promotion of Science (JSPS) through KAKENHI grant (18H05223, 20H00174, and 20H04737). This work is partly supported by the JSPS Open Partnership Bilateral Joint Research Project between Japan and Chile.

APPENDIX

A. NEWLY ADDED REFERENCE LIST FOR ^{56}Ni MASSES

Below, the newly added references to the reference list in Anderson (2019) are listed.

SNe II: Utrobin & Chugai (2011), Bose et al. (2018), Lisakov (2018), Singh et al. (2018, 2019a,b), Afsariardchi et al. (2019), Andrews et al. (2019), Buta & Keel (2019), Dastidar et al. (2019), Hillier & Dessart (2019), Martinez & Bersten (2019); Martinez et al. (2020), Meza et al. (2019), Ricks & Dwarkadas (2019), Szalai et al. (2019), Van Dyk et al. (2019), Bostroem et al. (2019, 2020), Gutiérrez et al. (2020a,b), Jäger et al. (2020), Sharon & Kushnir (2020), Müller-Bravo et al. (2020), Rodríguez et al. (2020), Zhang et al. (2020).

¹¹ Although there are many objects with $M_{\text{Ni}} \lesssim 10^{-3}M_{\odot}$ in the left panel of Fig.11, they are considered to be an artifact caused by an analytical fitting to the distribution, considering that there are no such objects in LS-SNe II (section 6).

753 SESNe: Margutti et al. (2017), Ashall et al. (2019), Fremling et al. (2019), Ho et al. (2019, 2020a,b), Nakaoka et
 754 al. (2019), Taddia et al. (2018, 2019a,b), Prentice et al. (2018, 2019, 2020b), Singh et al. (2019), Wang et al. (2019),
 755 Xiang et al. (2019), Moriya et al. (2020), Sharon & Kushnir (2020), Stritzinger et al. (2020).
 756 Ultra-stripped envelope SESNe candidates: Kasliwal et al. (2012) De et al. (2018), De et al. (2018), Yao et al.
 757 (2020), Prentice et al. (2020a).

REFERENCES

- 758 Afsariardchi, N., Moon, D.-S., Drout, M. R., et al. 2019,
 759 ApJ, 881, 22
- 760 Afsariardchi, N., Drout, M. R., Khatami, D., et al. 2020,
 761 arXiv:2009.06683
- 762 Anderson, J. P., Habergham, S. M., James, P. A., et al.
 763 2012, MNRAS, 424, 1372.
 764 doi:10.1111/j.1365-2966.2012.21324.x
- 765 Anderson, J. P. 2019, A&A, 628, A7
- 766 Andrews, J. E., Sand, D. J., Valenti, S., et al. 2019, ApJ,
 767 885, 43
- 768 Arnett, W. D. 1982, ApJ, 253, 785
- 769 Ashall, C., Mazzali, P. A., Pian, E., et al. 2019, MNRAS,
 770 487, 5824
- 771 Barnes, J., Duffell, P. C., Liu, Y., et al. 2018, ApJ, 860, 38
- 772 Bianco, F. B., Modjaz, M., Hicken, M., et al. 2014, ApJS,
 773 213, 19
- 774 Benvenuto, O. G., Bersten, M. C., & Nomoto, K. 2013,
 775 ApJ, 762, 74. doi:10.1088/0004-637X/762/2/74
- 776 Bersten, M. C., Benvenuto, O., & Hamuy, M. 2011, ApJ,
 777 729, 61
- 778 Bersten, M. C., Benvenuto, O. G., Folatelli, G., et al. 2014,
 779 AJ, 148, 68
- 780 Bose, S., Dong, S., Kochanek, C. S., et al. 2018, ApJ, 862,
 781 107
- 782 Bostroem, K. A., Valenti, S., Horesh, A., et al. 2019,
 783 MNRAS, 485, 5120. doi:10.1093/mnras/stz570
- 784 Bostroem, K. A., Valenti, S., Sand, D. J., et al. 2020, ApJ,
 785 895, 31
- 786 Buta, R. J. & Keel, W. C. 2019, MNRAS, 487, 832
- 787 Dastidar, R., Misra, K., Valenti, S., et al. 2019, MNRAS,
 788 490, 1605
- 789 De, K., Kasliwal, M. M., Ofek, E. O., et al. 2018, Science,
 790 362, 201
- 791 De, K., Kasliwal, M. M., Cantwell, T., et al. 2018, ApJ,
 792 866, 72. doi:10.3847/1538-4357/aadf8e
- 793 Drout, M. R., Chornock, R., Soderberg, A. M., et al. 2014,
 794 ApJ, 794, 23. doi:10.1088/0004-637X/794/1/23
- 795 Elmhamdi, A., Danziger, I. J., Chugai, N., et al. 2003,
 796 MNRAS, 338, 939
- 797 Falk, S. W., & Arnett, W. D. 1977, ApJS, 33, 515
- 798 Fang, Q., Maeda, K., Kuncarayakti, H., et al. 2019, Nature
 799 Astronomy, 3, 434. doi:10.1038/s41550-019-0710-6
- 800 Filippenko, A. V. 1997, ARA&A, 35, 309
- 801 Folatelli, G., Bersten, M. C., Benvenuto, O. G., et al. 2014,
 802 ApJL, 793, L22
- 803 Folatelli, G., Bersten, M. C., Kuncarayakti, H., et al. 2015,
 804 ApJ, 811, 147. doi:10.1088/0004-637X/811/2/147
- 805 Fremling, C., Ko, H., Dugas, A., et al. 2019, ApJL, 878, L5
- 806 Gangopadhyay, A., Misra, K., Sahu, D. K., et al. 2020,
 807 MNRAS, 497, 3770. doi:10.1093/mnras/staa1821
- 808 Georgy, C. 2012, A&A, 538, L8
- 809 Goldberg, J. A., Bildsten, L., & Paxton, B. 2019, ApJ, 879,
 810 3
- 811 Gräfener, G. & Vink, J. S. 2016, MNRAS, 455, 112
- 812 Gutiérrez, C. P., Sullivan, M., Martinez, L., et al. 2020,
 813 MNRAS, 496, 95
- 814 Gutiérrez, C. P., Pastorello, A., Jerkstrand, A., et al. 2020,
 815 MNRAS, 499, 974. doi:10.1093/mnras/staa2763
- 816 Hamuy, M. 2003, ApJ, 582, 905
- 817 Heger, A., Fryer, C. L., Woosley, S. E., et al. 2003, ApJ,
 818 591, 288
- 819 Hillier, D. J. & Dessart, L. 2019, A&A, 631, A8
- 820 Ho, A. Y. Q., Goldstein, D. A., Schulze, S., et al. 2019,
 821 ApJ, 887, 169
- 822 Ho, A. Y. Q., Corsi, A., Cenko, S. B., et al. 2020, ApJ, 893,
 823 132
- 824 Ho, A. Y. Q., Kulkarni, S. R., Perley, D. A., et al. 2020,
 825 ApJ, 902, 86. doi:10.3847/1538-4357/aba630
- 826 Ivezić, Ž., Kahn, S. M., Tyson, J. A., et al. 2019, ApJ, 873,
 827 111. doi:10.3847/1538-4357/ab042c
- 828 Jäger, Z., Vinkó, J., Bíró, B. I., et al. 2020, MNRAS, 496,
 829 3725
- 830 Kasliwal, M. M., Kulkarni, S. R., Gal-Yam, A., et al. 2010,
 831 ApJL, 723, L98
- 832 Kasliwal, M. M., Kulkarni, S. R., Gal-Yam, A., et al. 2012,
 833 ApJ, 755, 161. doi:10.1088/0004-637X/755/2/161
- 834 Kilpatrick, C. D., Takaro, T., Foley, R. J., et al. 2018,
 835 MNRAS, 480, 2072
- 836 Kushnir, D. 2015, arXiv:1506.02655
- 837 Lazzati, D., Morsony, B. J., Blackwell, C. H., et al. 2012,
 838 ApJ, 750, 68
- 839 Li, W., Leaman, J., Chornock, R., et al. 2011, MNRAS,
 840 412, 1441. doi:10.1111/j.1365-2966.2011.18160.x
- 841 Lisakov, S. 2018, Ph.D. Thesis

- Lyman, J. D., Bersier, D., James, P. A., et al. 2016, MNRAS, 457, 328
- Maeda, K., & Tominaga, N. 2009, MNRAS, 394, 1317
- Margutti, R., Kamble, A., Milisavljevic, D., et al. 2017, ApJ, 835, 140
- Martinez, L. & Bersten, M. C. 2019, A&A, 629, A124
- Martinez, L., Bersten, M. C., Anderson, J. P., et al. 2020, A&A, 642, A143. doi:10.1051/0004-6361/202038393
- Maund, J. R., Smartt, S. J., Kudritzki, R. P., et al. 2004, Nature, 427, 129
- Maund, J. R., Fraser, M., Ergon, M., et al. 2011, ApJL, 739, L37
- Maund, J. R. 2018, MNRAS, 476, 2629. doi:10.1093/mnras/sty093
- Meza, N., Prieto, J. L., Clocchiatti, A., et al. 2019, A&A, 629, A57
- Meza, N. & Anderson, J. P. 2020, A&A, 641, A177. doi:10.1051/0004-6361/201937113
- Milisavljevic, D., Patnaude, D. J., Raymond, J. C., et al. 2017, ApJ, 846, 50. doi:10.3847/1538-4357/aa7d9f
- Moriya, T. J. & Maeda, K. 2016, ApJ, 824, 100. doi:10.3847/0004-637X/824/2/100
- Moriya, T. J., Mazzali, P. A., Tominaga, N., et al. 2017, MNRAS, 466, 2085. doi:10.1093/mnras/stw3225
- Moriya, T. J., Suzuki, A., Takiwaki, T., et al. 2020, MNRAS, 497, 1619
- Müller, T., Prieto, J. L., Pejcha, O., et al. 2017, ApJ, 841, 127
- Müller-Bravo, T. E., Gutiérrez, C. P., Sullivan, M., et al. 2020, MNRAS, 497, 361
- Nakaoka, T., Moriya, T. J., Tanaka, M., et al. 2019, ApJ, 875, 76
- Ouchi, R. & Maeda, K. 2017, ApJ, 840, 90
- Pejcha, O., & Prieto, J. L. 2015, ApJ, 806, 225
- Prentice, S. J., Mazzali, P. A., Pian, E., et al. 2016, MNRAS, 458, 2973
- Prentice, S. J., Ashall, C., Mazzali, P. A., et al. 2018, MNRAS, 478, 4162
- Prentice, S. J., Ashall, C., James, P. A., et al. 2019, MNRAS, 485, 1559
- Prentice, S. J., Maguire, K., Flörs, A., et al. 2020, A&A, 635, A186. doi:10.1051/0004-6361/201936515
- Prentice, S. J., Maguire, K., Boian, I., et al. 2020, MNRAS, 499, 1450. doi:10.1093/mnras/staa2947
- Podsiadlowski, P., Joss, P. C., & Hsu, J. J. L. 1992, ApJ, 391, 246
- Pursiainen, M., Childress, M., Smith, M., et al. 2018, MNRAS, 481, 894. doi:10.1093/mnras/sty2309
- Reynolds, T. M., Fraser, M., Mattila, S., et al. 2020, MNRAS, 493, 1761
- Ricks, W. & Dwarkadas, V. V. 2019, ApJ, 880, 59
- Rodríguez, Ó., Pignata, G., Anderson, J. P., et al. 2020, MNRAS, 494, 5882
- Sawada, R., & Maeda, K. 2019, ApJ, 886, 47
- Shivvers, I., Zheng, W. K., Mauerhan, J., et al. 2016, MNRAS, 461, 3057
- Singh, A., Srivastav, S., Kumar, B., et al. 2018, MNRAS, 480, 2475
- Singh, A., Sahu, D. K., Anupama, G. C., et al. 2019, ApJL, 882, L15
- Singh, A., Kumar, B., Moriya, T. J., et al. 2019, ApJ, 882, 68
- Singh, M., Misra, K., Sahu, D. K., et al. 2019, MNRAS, 485, 5438
- Sharon, A. & Kushnir, D. 2020, MNRAS, 496, 4517
- Smartt, S. J. 2009, ARA&A, 47, 63
- Smartt, S. J., Eldridge, J. J., Crockett, R. M., et al. 2009, MNRAS, 395, 1409
- Smartt, S. J. 2015, PASA, 32, e016
- Smith, N., Li, W., Filippenko, A. V., et al. 2011, MNRAS, 412, 1522
- Stancliffe, R. J. & Eldridge, J. J. 2009, MNRAS, 396, 1699
- Stritzinger, M., & Leibundgut, B. 2005, A&A, 431, 423
- Stritzinger, M. D., Taddia, F., Holmbo, S., et al. 2020, A&A, 634, A21
- Suwa, Y., Yoshida, T., Shibata, M., et al. 2015, MNRAS, 454, 3073. doi:10.1093/mnras/stv2195
- Suwa, Y. & Tominaga, N. 2015, MNRAS, 451, 282
- Suwa, Y., Tominaga, N., & Maeda, K. 2019, MNRAS, 483, 3607
- Szalai, T., Vinkó, J., Könyves-Tóth, R., et al. 2019, ApJ, 876, 19
- Taddia, F., Sollerman, J., Leloudas, G., et al. 2015, A&A, 574, A60
- Taddia, F., Sollerman, J., Fremling, C., et al. 2018, A&A, 609, A106
- Taddia, F., Sollerman, J., Fremling, C., et al. 2019, A&A, 621, A64
- Taddia, F., Sollerman, J., Fremling, C., et al. 2019, A&A, 621, A71
- Tampo, Y., Tanaka, M., Maeda, K., et al. 2020, ApJ, 894, 27. doi:10.3847/1538-4357/ab7ccc
- Utrobin, V. P. & Chugai, N. N. 2011, A&A, 532, A100. doi:10.1051/0004-6361/201117137
- Valenti, S., Taubenberger, S., Pastorello, A., et al. 2012, ApJL, 749, L28. doi:10.1088/2041-8205/749/2/L28
- Vallely, P. J., Prieto, J. L., Stanek, K. Z., et al. 2018, MNRAS, 475, 2344. doi:10.1093/mnras/stx3303
- Van Dyk, S. D., Zheng, W., Fox, O. D., et al. 2014, AJ, 147, 37

- 942 Van Dyk, S. D., Zheng, W., Maund, J. R., et al. 2019, *ApJ*,
943 875, 136
- 944 Wang, S.-Q., Cano, Z., Li, L., et al. 2019, *ApJ*, 877, 20
- 945 Wang, S.-Q. & Li, L. 2020, *ApJ*, 900, 83.
946 doi:10.3847/1538-4357/aba6e9
- 947 Wheeler, J. C., Johnson, V., & Clocchiatti, A. 2015,
948 *MNRAS*, 450, 1295
- 949 Woosley, S. E., Eastman, R. G., Weaver, T. A., et al. 1994,
950 *ApJ*, 429, 300. doi:10.1086/174319
- 951 Woosley, S. E., Heger, A., & Weaver, T. A. 2002, *Reviews*
952 *of Modern Physics*, 74, 1015
- 953 Xiang, D., Wang, X., Mo, J., et al. 2019, *ApJ*, 871, 176
- 954 Yao, Y., De, K., Kasliwal, M. M., et al. 2020, *ApJ*, 900, 46
- 955 Yoon, S.-C., Woosley, S. E., & Langer, N. 2010, *ApJ*, 725,
956 940
- 957 Yoon, S.-C., Dessart, L., & Clocchiatti, A. 2017, *ApJ*, 840,
958 10
- 959 Zhang, J., Wang, X., József, V., et al. 2020, *MNRAS*, 498,
960 84. doi:10.1093/mnras/staa2273